The effect on the lunar exosphere of a coronal mass ejection passage

R. M. Killen,[1,3] D. M. Hurley,[2,3] and W. M. Farrell[1,3]

[1] Solar wind bombardment onto exposed surfaces in the solar system produces an energetic component to the exospheres about those bodies. The solar wind energy and composition are highly dependent on the origin of the plasma. Therefore, using the measured composition of the slow wind, fast wind, solar energetic particle (SEP) population, and coronal mass ejection (CME), we have estimated the total sputter yield for each type of solar wind. We show that the heavy ions, especially the He^{++} and O^{+7}, can greatly enhance the total sputter yield during times when the heavy ion population is enhanced. Folding in the flux with the yield of individual ions, we compute the source rate for several species during different types of solar wind. Finally, we use a Monte Carlo model developed to simulate the time-dependent evolution of the lunar exosphere to study the sputtering component of the exosphere under the influence of a CME passage. We simulate the background exosphere of Na, K, Ca, and Mg. Simulations indicate that sputtering increases the mass of those constituents in the exosphere more than ten times the background values. The escalation of atmospheric density occurs within an hour of onset. The decrease in atmospheric density after the CME passage is also rapid, although takes longer than the increase. Sputtered neutral particles have a high probability of escaping the Moon, by both leaving the Hill Sphere and photoionization. Density and spatial distribution of the exosphere can be tested with the LADEE mission.

Citation: Killen, R. M., D. M. Hurley, and W. M. Farrell (2012), The effect on the lunar exosphere of a coronal mass ejection passage, *J. Geophys. Res.*, *117*, E00K02, doi:10.1029/2011JE004011.

1. Introduction

[2] The lunar exosphere is, in a sense, the visible interface between the lunar surface and the interplanetary medium. Volatiles are degassed due to the effect of the solar flux onto the surface, and both volatile and less volatile material can be ejected from the surface by more energetic and violent processes such as sputtering by the solar wind, and by hypervelocity impact of dust, meteoroids and, less often, asteroids and comets. Transport of volatiles through the exosphere can lead to cold-trapping of volatiles in the polar regions, and less permanent sequestration of volatiles on the nightside. These processes are of practical interest to lunar explorers who may rely on polar-trapped volatiles, and to those interested in space weather related phenomena that may impact earth-orbiting spacecraft.

[3] The lunar exosphere is sparse and highly variable. The multiple mechanisms releasing constituents from the surface into the exosphere are time-varying, often with comparable release rates. Meanwhile, lifetimes of particles in the atmosphere of the Moon are similar to the timescale of the variability in the sources. Thus transient phenomena are capable of contributing the bulk of the total atmosphere. In fact, the volatiles released by an Apollo landed mission doubled the total atmospheric mass of the Moon temporarily [*Vondrak*, 1992]. One such transient phenomenon is the sputtering of excess material into the atmosphere from an interplanetary coronal mass ejection (ICME). Although sputtering does not provide the bulk of the lunar atmosphere during normal conditions, we consider the enhancement that might result when an ICME impacts the lunar surface. Increased space weathering events during the active phase of the solar cycle may lead to more rapid cold-trapping of volatiles.

[4] Furthermore, the exosphere is a source of ions in the solar wind interaction with the Moon [e.g., *Winske et al.*, 1985; *Cladis et al.*, 1994]. Neutrals in the lunar exosphere are subject to ionization by photons, protons, and electrons. Once ionized, they are accelerated by the motional electric field of the solar wind and influence the solar wind interaction through momentum transfer to the solar wind and plasma instabilities. The Solar Storm-Lunar Atmosphere Modeling (SSLAM) Lunar Extreme Workshop (LEW) investigated the entire lunar surface-exosphere-space plasma system during a space weather event at the Moon (W. M. Farrell et al., Solar-Storm/Lunar Atmosphere Model (SSLAM): An overview of the effort and description of the

[1]Planetary Magnetospheres Branch, NASA Goddard Space Flight Center, Greenbelt, Maryland, USA.
[2]Johns Hopkins University Applied Physics Laboratory, Laurel, Maryland, USA.
[3]NASA Lunar Science Institute, Moffett Field, California, USA.

driving storm environment, submitted to *Journal of Geophysical Research*, 2012). The SSLAM LEW followed the effects of the solar storm of 2 May 1998 from its effects on the lunar surface (D. M. Hurley et al., Solar wind contribution to the hydroxyl and water features on the lunar surface, submitted to *Journal of Geophysical Research*, 2012), through the exosphere (this paper), the exo-ionosphere (M. Sarantos et al., Ions in the lunar exosphere and wake resulting from a CME passage, submitted to *Journal of Geophysical Research*, 2012), to the plasma interaction (D. Krauss-Varban and P. Travnicek, Hybrid simulation of a CME-driven Moon, submitted to *Journal of Geophysical Research*, 2012) and the resulting electromagnetic environment (M. Zimmerman et al., Plasma wake simulations and object charging in a shadowed lunar crater during a solar storm, submitted to *Journal of Geophysical Research*, 2012; W. M. Farrell et al., The solar storm effect on the lunar photoelectric sheath and precursor region: A change in trapping efficiency, submitted to *Journal of Geophysical Research*, 2012) and its effects on dust (T. J. Stubbs et al., Surface charging and dust transport predictions during a solar storm, manuscript in preparation, 2012; D. Glenar and T. Stubbs, Spectroscopic changes in lunar horizon glow during a CME passage, submitted to *Journal of Geophysical Research*, 2012). SSLAM provided the opportunity to examine feedback between the components of the system. This paper presents simulations of the effects of the solar storm on the exosphere, which is derived from the surface and provides feedback for the plasma environment. We have modeled the volatile species that have been observed from the ground (Na and K) and the refractory species that have been observed in Mercury's exosphere (Ca and Mg) and are expected to be observed at the Moon. We have not modeled the noble gases, Ar and He, nor have we modeled H. These species behave differently than those that are derived from the rocks. Argon, which was measured by the mass spectrometer, The Lunar Atmospheric Composition Experiment (LACE), deployed on *Apollo 17* is believed to diffuse to the surface following decay of ^{40}K. Both H and He, also measured by LACE, are derived from the solar wind, but in addition ^{4}He may be outgassed from the interior. These species will be considered in a subsequent paper.

[5] Because the morphology of the exosphere is a function not only of the rate at which atoms are ejected, but also their energy distributions, radiation pressure, thermal accommodation, sticking at the surface, and possible chemical reactivity, we consider four species: Na, K, Mg, and Ca. The first two species are known to exist about the Moon, having been observed by ground-based telescopes [*Potter and Morgan*, 1985, 1988a], and the latter two are known to exist at Mercury [*Bida et al.*, 2000; *McClintock et al.*, 2009] and are expected to also exist at the Moon. Mg and Ca have not yet been detected in the ambient lunar exosphere [*Stern*, 1999], although they were detected in the vapor plume after the Lunar Crater Observation and Sensing Satellite (LCROSS) impact [*Gladstone et al.*, 2010]. We use the measured solar wind composition, density and velocity for various solar wind types, and we use the most recent information on sputtering by highly charged ions. We first describe the Monte Carlo model, then we describe the solar wind

measurements and sputtering values that we employ, and next we show the models for the four species considered.

2. Lunar Atmospheric Model

2.1. Model History and Background

[6] In a surface-bounded exosphere, particles are not expected to interact with other exospheric particles, but only interact with the surface [*Stern*, 1999; *Killen et al.*, 2007]. Because the exosphere is collisionless, different species or different sources of a single species can be modeled separately using Monte Carlo techniques without having to incorporate interactions. This makes Monte Carlo modeling a useful tool for deciphering important physical processes at play in the creation and maintenance not only of the lunar exosphere but also of other exospheres in the solar system, including those at Mercury, Io and Europa.

[7] Although photon-stimulated desorption (PSD) has been shown to provide the bulk of the lunar Na and K atmosphere during normal conditions, we consider the enhancement that might result when a CME impacts the lunar surface. Because the morphology of the exosphere is a function not only of the rate at which atoms are ejected, but also their energy distributions, radiation pressure, thermal accommodation and sticking at the surface, and possible chemical reactivity, we consider four species, Na and K which are volatiles, and Mg and Ca which are more refractory.

[8] *Crider and Vondrak* [2000, 2002] developed a Monte Carlo model of the migration of particles in a surface bounded exosphere for application to the Moon similar to those developed by others [see *Hodges*, 1973; *Arnold*, 1979; *Butler*, 1997] and those used to study the exosphere of Mercury [*Wurz and Lammer*, 2003; *Leblanc and Johnson*, 2010; *Mura*, 2011]. The model follows the path of a particle under the effects of gravity and radiation pressure once it is released into the exosphere with an energy selected from a distribution function for the selected source process (section 2.2). In flight, one of three things can happen. The particle may escape the planet's gravitational field, may be photoionized or photodissociated, or may return to the surface. For the particles that return to the surface intact, they may bounce elastically for another ballistic hop, they may thermalize or exchange energy with the surface and be released with a new energy, or they may stick to the surface. At some point, the particles will be lost from the atmosphere, will arrive in a cold trap, or will stick (chemisorb). The Monte Carlo model records particle positions and velocities at user-defined times, flux to specific points on the surface, and loss rates. Most components of the model are modular such that various sources, losses, and physics can be selected by the user to explore the effects these have on the atmosphere. These modules are described in the following subsections.

2.2. Model Description

2.2.1. Ballistic Motion

[9] After release from the surface at a given position with velocity vector selected from an appropriate distribution function, as discussed below, the model calculates the particle's trajectory under gravity and radiation pressure using a fourth order Runge-Kutta (RK-4) algorithm. Migrating particles follow a ballistic trajectory once released from the

surface because the lunar atmosphere is collisionless. Without radiation pressure, the final position and time of flight can be found analytically assuming a spherical Moon [*Vogel*, 1966]. Earlier lunar publications using this model have only used the analytic function and no radiation pressure [*Crider and Vondrak*, 2000; 2002]. At Mercury, radiation pressure is significant, especially for Na and K [see *Potter et al.*, 2007] whereas at the Moon, the radiation pressure is less important and can be ignored unless one is studying the lunar tail region [e.g., *Smyth and Marconi*, 1995a, 1995b]. The RK-4 algorithm has been implemented to follow the trajectory of the particles using the equation of motion [*Killen et al.*, 2010; *Hurley*, 2011]. The results presented here use the equation of motion, but neglect radiation pressure and the effects of surface charging.

[10] The current model assumes the Moon is a sphere with radius 1738 km. There are large-scale topographic features that might affect bulk properties of the atmosphere, but at present are not modeled except for cold traps. Small-scale effects, i.e., the "fairy castle" effect [*Hapke and Cassidy*, 1978] also are not considered directly in the present work.

2.2.2. Source Functions

[11] The Monte Carlo model of the migrating gases takes a source function (including spatial and energy distributions) and simulates the trajectories of large numbers of particles (10^5-10^6). It is able to incorporate the different source functions required for the different processes at work on the Moon, including photon-stimulated desorption, thermal desorption, ion sputtering, micrometeoroid release, outgassing, or large impact events [see, e.g., *Killen and Ip*, 1999].

[12] An input flux and spatial distribution is assigned as appropriate for the source: solar UV radiation for photon-stimulated desorption, solar particle flux for ion sputtering, and micrometeoritic or meteoritic flux for impact vaporization. At the Moon, solar wind flux dies off with solar zenith angle due to the curvature of the Moon, unlike at Mercury where the solar wind flux onto the surface depends on the locus of open magnetic field lines, which is highly variable. Ion flux is greatly reduced on the night side of the Moon [*Ogilvie et al.*, 1996]. When the Moon is inside the earth's magnetosphere it is shielded from the solar wind, but it may traverse the plasma sheet, which contains high-energy plasma rich in oxygen ions from the Earth. Micrometeorite release, in contrast, is expected to be isotropic over the surface of the Moon, at least within a factor of two. A cometary impact or asteroid impact is localized to a specific position, and meteor streams are directional.

[13] The ejected products are assigned an initial velocity from the surface drawn from the distribution function appropriate to the release mechanism [*Hofer*, 1991; *Roth*, 1983]. Both source processes and surface interactions are species-dependent, resulting in various energies and compositions of the ejected products. The solar wind ions implant themselves into the regolith and cause physical and chemical sputtering with an efficiency dependent on their kinetic and potential energy. Physical sputtering and back-scattering are relatively high-energy release mechanisms, whereas chemical sputtering and thermal processes eject atoms at lower energies on average.

[14] In order to correlate the source rate with an atmospheric distribution, we assign a start time to the particles in the simulation at random within a specified time window. This introduces a source rate into the model (the number of simulation particles in a simulation time window), which enables scaling to a physical source rate after running. This is possible because of the collisionless nature of the exosphere. Each modeled source is described below.

2.2.2.1. Photon-Stimulated Desorption

[15] Photon-stimulated desorption (PSD) was first suggested as a source for Mercury's sodium exosphere by *McGrath et al.* [1986], and subsequently as a source for the lunar sodium exosphere [*Potter and Morgan*, 1988b]. Subsequent laboratory work used electron-stimulated desorption as a proxy for PSD to establish a desorption cross section of $Q = (3 \pm 1) \times 10^{-20}$ cm^2 at 5 eV [*Yakshinskiy and Madey*, 1999]. The solar flux at $h\nu > 5$eV is 2×10^{14} photons cm^{-2} s^{-1} and the surface number density of Na atoms, σ, is about 3×10^{12} cm^{-2}. The PSD source flux calculated using this rate would be

$$F^{PSD} = F_{ph} \cos(\psi) Q \sigma / R^2, \tag{1}$$

where F_{ph} is the solar flux at $h\nu > 5$eV at Earth orbit, f_{Na} is the fraction of sodium atoms in the regolith, σ is the Na surface coverage, taken to be $f_{Na} \times 7.4 \times 10^{14}$ cm^{-2}, ψ is the solar zenith angle, and R is the distance from the sun. The fractional abundance of lunar sodium is 0.005. The theoretical cross section for PSD desorption was determined to be overly efficient unless the loss processes for Na were also extremely efficient [e.g., *Killen et al.*, 2001]. *Cassidy and Johnson* [2005] calculated a correction factor of a factor of three to account for trapping of the ejected atoms in the regolith. In this model, we consider PSD yields beginning with the *Yakshinskiy and Madey* [1999] yield reduced by a factor of three as suggested by *Cassidy and Johnson* [2005], and subsequently consider the consequences of further reduction of yields in the absence of ion- flux to the surface, and of an ion-flux enhancement of those baseline yields. Observations of the lunar exosphere inside the Earth's magnetosphere [*Potter et al.*, 2000] supported a feedback between ion impact and photon-stimulated desorption [e.g., *Sarantos et al.*, 2008, 2010], most likely due to defect enhanced diffusion caused by ion impacts. *Sarantos et al.* [2008, 2010] suggested that the effective PSD yields consistent with the observations were reduced by up to a factor of six from the experimental PSD yield by *Yakshinskiy and Madey* [1999]. The velocity of a particle released by PSD is taken from a thermal velocity distribution with a temperature of 1200 K.

2.2.2.2. Impact Vaporization

[16] Vaporization due to meteoritic impact was considered as a possible source of the sodium and potassium exospheres of Mercury [*Morgan et al.*, 1988; *Cremonese et al.*, 2005] and for the Moon [*Potter and Morgan*, 1988b]. The importance of impact vaporization was shown by *Hunten et al.* [1998] who observed a brightening of the lunar sodium tail after the passage of the Moon through the Leonid meteor stream. Impact-induced exospheres produced by micrometeoritic debris of mass < 0.1 g were modeled for both Mercury and the Moon by *Cintala* [1992]. More recently, meteors of mass > 0.1 g were considered as sources of a transient atmosphere [*Mangano et al.*, 2007].

Table 1. Enthalpy of Vaporization for Various Minerals, Metals and Oxides

Material	Enthalpy of Vaporization (MJ/kg)
FeS	1.150
Fe	6.272
Diabase	8.500
Regolith	9.643
MgO	10.46
SiO$_2$	20.93

[17] This model for impact vaporization is based on the impedance matching method [*Melosh*, 1989; *Morgan and Killen*, 1998; *Killen*, 2003] and the total influx is an input parameter.

[18] Some differences in the current impact-vaporization code from that described by *Morgan and Killen* [1998] are that the peak pressure of the impact is calculated using the equations given by *Melosh* [1989], chapters 3 and 4, and not using the approximation described by *Lange and Ahrens* [1987]. The peak pressure, P$_p$, is given by

$$P_p = r(C_t u_t + S_t u_t^2), \qquad (2)$$

where r is the density in the target, u$_t$ is the change in particle velocity across the shock in the target, C$_t$ has dimensions of velocity and is empirically determined, and S$_t$ is dimensionless and is also empirically determined. The constants C and S for the target and impactor are input parameters and can be found in the work of *Melosh* [1989, Table AII.2] for various materials such as iron, diabase, sandstone, quartz, dunite and water. In addition to these parameters the critical pressure for vaporization is a function of enthalpy required for vaporization, H$_v$, which is an input parameter, for these runs set to that for regolith determined by *Cintala* [1992]. The temperature at which a given constituent vapor boils off a mineral is the temperature of vaporization of the individual component [*Ahrens and O'Keefe*, 1972]. Thus the more volatile components will vaporize first, at significantly lower impact velocities than those required for complete vaporization. We estimate the critical pressure for vaporization of individual gases by scaling the critical pressure for vaporization of regolith as defined by *Cintala* [1992] by the ratio of the enthalpies required for vaporization [*Chase et al.*, 1985], given in Table 1. Our function for the minimum impact velocity required for vaporization has the form of a quadratic:

$$v_{min} = a + b \cdot m + c \cdot m^2, \qquad (3)$$

where the constants a, b and c are given in Table 2 as a function of rock type and impactor type, and m is distension, or m = 1/(1-ρ), where ρ is porosity. Distension varies from 1.8 for the uppermost tens of cm of regolith to 1.1 at about 1 km depth. Aluminum was chosen as the impactor because the properties of aluminum are closest to those of stony-iron meteorites, and it has been used in many laboratory tests. The mean velocity of expansion of a vapor cloud created from a hyper-velocity impact is twice the sound speed in the medium regardless of the impact velocity. For regolith the sound speed is about 1.3 km/sec, thus the expansion velocity

is on the order of 2 km/sec [*Schultz*, 1996], comparable to lunar escape velocity, 2.38 km/sec. The temperature derived from this expansion speed is 5566 K. Because collisions with the regolith may decrease the expansion velocity, the simulations shown in this paper assume a vapor temperature of 3000 K.

[19] The observation of a 3000 K lunar exosphere at minimum column abundance inside the Earth's magnetosphere was interpreted by *Sarantos et al.* [2008] to constrain the impact vapor source at the Moon to approximately ≤ 8.5 × 10^4 cm^{-2} s^{-1}, given a residence time in the lunar exosphere of 6000 s from our Monte Carlo modeling.

2.2.2.3. Ion Sputtering

[20] *Potter and Morgan* [1988b] recognized that a sputter source could produce the very extended lunar sodium exosphere. Sputtering of Na by solar wind ions impinging onto the surface of Mercury through the cusps of the magnetosphere was suggested by *Potter and Morgan* [1990] to explain rapid variations in the observed Na exosphere, with high to midlatitude enhancements appearing and disappearing on intervals less than a day. At Mercury, the solar wind only impacts the surface along open field lines, or near the open-closed boundary region [*Sarantos et al.*, 2007; *Kallio and Janhunen*, 2003], but the solar wind impacts the entire sunward side of the Moon whenever the Moon is outside of the Earth's magnetosphere. Kinetic energies of solar wind ions are on average 1 keV/amu, near where the sputtering efficiency peaks [*Johnson*, 1990]. Sputtering by H$^+$, which normally accounts for 85% of the total kinetic energy carried by the solar wind, is relatively inefficient. He^{2+} accounts for about 13% of the kinetic energy carried by the normal (slow and fast) solar wind, and is generally assumed to account for most of the space weathering effects. In addition, although heavy ions (Z > 6) account for only about 2% of the kinetic energy carried by the normal solar wind, they also carry ~1 keV each in potential energy due to ionization [*Krachner et al.*, 2003]. The sputter yield of protons is low, and the fraction of heavy ions in the slow and fast solar wind is low. However, the fraction of heavy ions in the solar wind increases dramatically in a CME or solar magnetic cloud. Sputtering yields by heavy ions have been considered both theoretically [*Sporn et al.*, 1997; *Shemansky*, 2003; *Kallio et al.*, 2008] and experimentally [*Meyer et al.*, 2011] and have been shown to be orders of magnitude more efficient than sputtering by protons.

[21] The charge state of the impinging ion has little effect on the sputter efficiency of highly conducting targets (conductors and semiconductors), but has considerable effect on insulators [*Aumayr and Winter*, 2004]. Sputtering of surfaces by highly charged projectiles in which the potential energy of ionization contributes significantly to the yield is called potential sputtering. Models for potential sputtering

Table 2. Parameters to Fit the Minimum Impact Velocity as a Function of Distension

Mineral	a	b	c
Al - enstatite	21.014	−14.154	3.058
Al - dunite	28.214	−27.23	7.812
Fe - enstatite	16.657	−11.371	2.5
Fe - dunite	18.893	−17.034	4.866

predict the formation of a short-lived multiply excited atom with highly excited outer shell electrons, and with some empty inner shells. Potential energy of the projectile is converted into kinetic energy of emitted electrons and electronic excitation of a small surface area. In insulator targets, in which perturbations of the electronic structure cannot be rapidly dissipated within the target, structural surface modifications result: defect formation, desorption and sputtering. Measured sputter yields of 1.5 keV Xe^{q+} onto Al_2O_3 show an approximately 40-fold increase in the sputter yield due to Xe^{28+} over that of Xe^{9+}, and yields of SiO_2 bombarded by 1 keV Ar^{q+} show a 2.6-fold increase in yield for Ar^{8+} over those of Ar^+. Both of these materials appear to have a finite sputter yield at zero kinetic energy of the projectile. On the other hand, for a highly ionic oxide such as MgO, even though potential energy greatly increases the sputter yield, potential energy does not induce sputtering in the absence of kinetic energy of the projectile. *Okabayashi et al.* [2005] studied secondary ion emission from solid surfaces irradiated with highly charged ions. In the case of a water adsorbed Si surface, they found that the yield of H^+ strongly depended on the charge state of the projectile, but that the yield of Si^+ is independent of the charge for Ar^{q+} projectiles. Si^+ and $SiOH^+$ ions were therefore ejected primarily by a kinetic sputtering process.

[22] The normalized energy distribution for particles sputtered from a solid, $f(E_e)$, with the energy E_e of the sputtered particle, has been given as [*Sigmund*, 1969]

$$f(E_e) = \frac{6E_b}{3 - 8\sqrt{E_b/E_c}} \frac{E_e}{(E_e + E_b)^3} \left\{ 1 - \sqrt{\frac{E_e + E_b}{E_c}} \right\}, \quad (4)$$

where E_b is the surface binding energy of the sputtered particle and E_c is the cut-off energy for sputtered atoms. The cut-off E_c, which is the maximum energy that can be imparted to a sputtered particle by a projectile particle with energy E_i, is given by the limit imposed by a binary collision between a projectile atom, m_1, and the target atom, m_2, (to be sputtered) as

$$E_c = E_i \frac{4m_1 m_2}{(m_1 + m_2)^2}. \quad (5)$$

For potential sputtering the maximum energy would probably be increased.

2.2.3. Surface Interaction

[23] When the particle comes back into contact with the surface, there are a variety of processes that can occur. These surface-atmosphere interactions in the extreme vacuum environment of atmosphereless bodies introduce an array of interesting physics questions that are still not well-studied, but can have an effect on atmospheric distribution. When the atmospheric particle reencounters the planet, it may stick to the surface (discussed in section 2.2.4). It may adsorb to the surface long enough to partially or fully thermalize to the local surface temperature and then be re-emitted. Or it may rebound on contact retaining all or most of its incident energy. We have assumed herein that Ca and Mg stick upon contact with the surface.

[24] The energy exchange at the surface for particles that return to the surface and are re-emitted is parameterized by a thermalization coefficient (w) and a conservation coefficient (f) that governs the energy exchange between the particle and the surface. The weights applied to v_t, a velocity from the Maxwellian distribution at the local surface temperature (thermal accommodation) and to v_i the incident particle velocity (rebound) total unity. The inbound and thermal velocities are added in quadrature with appropriate weights to compute the outbound velocity. The conservation coefficient is applied afterward to provide a separate means of damping particles:

$$v_f = \sqrt{f\left(wv_t^2 + (1 - w)v_i^2\right)} \quad (6)$$

[25] In all of the work presented here, we assume f = 1, i.e., there is no separate damping of energy. All of the energy exchange with the surface occurs through the thermal accommodation. We used values of 0.2 and 0.5 for w as explained below.

[26] If a particle is re-emitted, the direction of release occurs with an isotropic angular distribution. However, given the microstructure of the regolith, this is a simplification. The re-emitted particle is followed on all of its ballistic hops until it is lost from the system either to sticking, escape, or photoionization.

[27] We assume that Mg and Ca stick with 100% efficiency, which is appropriate for a refractory species. K sticks with 100% efficiency for T < 200 K. For T > 200 K, the accommodation coefficient is 0.5. I.e., the energy of the particle on rerelease from the surface is weighted half by the rebound energy and half by the energy associated with the local temperature. Na sticks with 100% efficiency for T < 200 K. For T > 200 K, the accommodation coefficient is 0.2—20% thermal and 80% rebound. This value of thermal accommodation is consistent with that found by *Mouawad et al.* [2011] for Na at Mercury. Also for Na, only half of the particles that stick where the surface temperature drops below 200 K are reemitted when the temperature rises. In contrast all of the "stuck" K are reemitted when the temperature rises.

2.2.4. Loss Processes
2.2.4.1. Sticking

[28] When the particle encounters the surface, the code determines whether the particle will stick or be re-emitted depending on the sticking functions assigned to the simulation. If there is no sticking, the particle is re-emitted as described in section 2.2.3 until it is lost by some other process. For cold-trap sticking, the particle sticks if it lands in a cold-trap location as defined in the simulation. The probability of sticking depends on the surface temperature for temperature-dependent sticking.

[29] For the Moon, we approximate the surface temperature (in Kelvin) by the function

$$T = 300 \cos^{1/4} \theta + 100, \text{ for } \theta < 90° \\ = 100, \text{ for } \theta > 90° \quad (7)$$

where T is the surface temperature and θ is the solar zenith angle.

[30] For long-term sticking, the probability of sticking could be a function of temperature or could be based on the surface composition. The user specifies a probability

Table 3. Physical Parameters for the Moon and Mercury

Body	Moon	Mercury
Vesc (km/s)	2.376	4.25
g (m/s^2)	1.624	3.8
Radius (km)	1738	2438
Tphot (Na)	1.689E5	1.689E5 R^2_{orbit}
Tphot (K)	4.510E4	4.510E4 R^2_{orbit}
Tphot (Ca)	1.429E4	1.429E4 R^2_{orbit}
Tphot (Mg)	1.770E6	1.770E6 R^2_{orbit}

Table 4. Source Rate (s^{-1}) for Each Species and Process Included in the Simulations Presented in Figures 1–5

Species	PSD	Impact Vaporization	Slow SW	CME
Na	9.49E21	1.79E21	8.54E21	4.65E23
K	3.80E21	2.81E20	2.94E21	1.71E23
Ca		2.95E22	9.30E22	5.03E24
Mg		3.08E22	7.78E22	4.18E24

function for sticking that can be based on the temperature, can be a day-night functionality, can allow for a set number of bounces before sticking, can allow no sticking, or can be a fixed probability where sticking is queried on every return to the surface. If a particle sticks to the surface in the code, its time and position are recorded. This output is then available as input for other runs where the distribution of adsorbed particles needs to be known. Alternatively, the code can immediately consider the later reemission of a stuck particle. For example, when nightside sticking is enabled, the code can assume that the particle is re-emitted at the dawn terminator by a specified release process (thermal desorption or photon-stimulated desorption). This way, one can follow a particle until it is lost from the planet by escape or photo-ionization rather than just recycling to the regolith.

[31] In these simulations, sticking is applied as a temperature-based function. For each time the particle comes into contact with the surface, the local surface temperature is queried. If the temperature is below the setting, the particle sticks.

2.2.4.2. Photoionization

[32] Photoionization rates depend on the ionization potential of the atom in question, and also on the solar flux available with energy at or exceeding the ionization energy. Since most of this energy comes in the form of UV radiation, the rate is dependent on the solar flux. The solar UV flux is currently available on the LISIRD website (lasp.colorado.edu/LISIRD) [*Snow et al.*, 2005]. We use the ionization cross sections computed by *Huebner et al.* [1992] either for quiet sun or for active sun, scaled to the orbital distance of the planet or Moon at the time of observation. The rates are summarized in Table 3. For sodium, there has been a controversy about the photoionization rate, since the theoretical cross section from *Chang and Kelly* [1975] and the experimental cross section from *Hudson* [1964] and *Hudson and Carter* [1967] differ by a factor of 2.7. Both *Huebner et al.* [1992] and *Combi et al.* [1997] recommend the theoretical cross section derived by *Chang and Kelly* [1975]. We have therefore adopted the theoretical cross section. *Huebner et al.* [1992] did not publish a photoionization rate for calcium. However, Huebner calculated a rate of 7.0×10^{-5} s^{-1} at quiet sun and 7.8×10^{-5} s^{-1} for active sun. The corresponding excess energies of the electrons are 0.38 eV and 0.47 eV, respectively (W. Huebner, personal communication, 2003).

[33] The probability of photoionization or photodissociation during a given ballistic hop is based on the photoionization time [*Huebner et al.*, 1992; *Verner et al.*, 1996] and the time of flight in sunlight.

2.2.4.3. Jeans Escape

[34] The particle escapes the simulation when it crosses a predetermined boundary. The Hill sphere is at 35 radii, where the gravitational pull of Earth exceeds that of the Moon. The simulations stop tracking particles once they reach the Hill sphere.

2.3. Steady State and Time-Dependent Models

[35] The model is run for many particles (usually 1 million) with a spatial and energy distribution matching the release mechanism. The positions and velocities of the particles are recorded at pre-determined time steps. For steady state, one weights each model particle by the source rate (Table 4). In steady state, the output time cadence is 1-min intervals. For the time dependent runs, a time cadence of 10 min was chosen. At each time step, particles are weighted by the source rates from a time-profile. Binning the weighted model particles by volume produces density. Similarly, binning along a line of sight computes column density.

3. CME Passage

[36] We have computed the total sputter yield on the lunar surface for an element normal to the solar wind (i.e., there are no geometrical effects included.) The solar wind types considered are fast wind, slow wind, and CME shock, bubble and driver gas. The density, velocity and fraction of He^{++} assumed for each of these wind types are given in Table 5. To be consistent with the definitions given by Farrell et al. (submitted manuscript, 2012), the CME 'shock' plasma is defined as the warm plasma immediately following the passage of the interplanetary shock but before actually passage into the CME (Interval 2 in the work of Farrell et al. (submitted manuscript, 2012)). The magnetic bubble period is that also called the 'early CME' period when the B-field is relatively strong in the CME but the plasma is of relatively low density (Interval 3 in the work of Farrell et al. (submitted manuscript, 2012)). The driver gas period is also referred to as the 'late CME' when the plasma becomes very dense (Interval 4 in the work of Farrell et al. (submitted manuscript, 2012)). The enrichment of heavy ions is species

Table 5. Density, Velocity and He^{++} Fraction Assumed for Wind Types

Wind Type	f(He^{++})	Density (cm^{-3})	Velocity (km/s)
Fast	0.02	5	450
Slow	0.04	5	450
Shock	0.001	20	600
Magnetic bubble	0.100	3	650
CME driver gas	0.300	70	500

Table 6. Composition of the Solar Wind, Shock, Magnetic Bubble and Driver Gas Assumed

Species Ratio	Fast Wind	Slow Wind	Shock	Magnetic Bubble	Driver Gas
Alpha/proton	0.02	0.04	0.001	0.10	0.30
O/He	0.0137	0.0119	0.0322	0.0322	0.0322
O/proton	2.74E-4	4.86E-4	3.22E05	3.22E-4	9.66E-3
C/O	0.683	0.670	0.380	0.380	0.380
C/proton	1.87E-4	3.19E-4	1.22E-5	1.22E-4	3.67E-3
N/O	0.111	0.088	0.08	0.08	0.08
N/proton	3.04E-5	4.19E-5	2.58E-6	2.58E-5	7.73E-4
Ne/O	0.082	0.104	0.32	0.32	0.32
Ne/proton	2.25E-5	4.95E-5	1.03E-5	1.03E-4	3.09E-3
Mg/O	0.105	0.143	0.29	0.29	0.29
Mg/proton	2.88E-5	6.81E-5	9.34E-6	9.34E-5	2.80E-3
Si/O	0.115	0.132	0.18	0.18	0.18
Si/proton	3.15E-5	6.28E-5	5.80E-6	5.80E-5	1.74E-3
S/O	0.056	0.051	0.122	0.122	0.122
S/proton	1.53E-5	2.43E-5	3.93E-6	3.93E-5	1.18E-3
Fe/O	0.092	0.106	0.73	0.73	0.73
Fe/proton	2.52E-5	5.05E-5	2.35E-5	2.35E-4	7.05E-3

dependent, as listed in Table 6. Both the magnetic bubble and CME driver gas are highly enriched in heavy ions. Even in spite of the low density in the bubble, the sputter yield is substantially increased above that in the solar wind. The composition of the fast solar wind and slow wind are from *von Steiger et al.* [2000] for south (fast wind) and minimum (slow wind). Abundance ratios were all given relative to O. The Ne/O and Mg/O ratios were found to vary from 0.26 to 0.38 for Ne/O and from 0.23 to 0.36 for Mg/O for central events in ICMEs depending on whether the associated flare is none, C-flare, M-flare or X-flare, with X-flare being the most intense and having the most enhanced Ne and Mg abundances. The values in Table 6 are for the M-flare associated Interplanetary CME (ICME) [*Reinard*, 2008]. The values for S/O and Fe/O are from *Wurz et al.* [1997]. Note that *Carter et al.* [2010] give the Si XIII/O VIII flux as 0.3 whereas the Si XIV/O VIII flux is given as 0.15. We have used the intermediate value of 0.18 consistent with the *Wurz et al.* [2000] report that Si/O is elevated by a factor of 1.55 in the January 6, 1997, CME. Although *Gloeckler et al.* [1999] report that the Si/O and Mg/O ratios in the May 1998 CME were consistent with those typical of the slow solar wind, the more usual state is for these ions to be elevated by up to a factor of two in CMEs. We did not find information on the composition of the shock and magnetic bubble except for the alpha/proton and O/He. Therefore we used the same composition for the heavier ions for the three components of the CME.

[37] Kinetic sputtering, a process in which kinetic energy is transferred from the incoming ions to the substrate, resulting in the ejection of atoms and ions, is relatively well understood. This is the dominant sputtering mechanism for

metals and semiconductors. However, on insulating surfaces such as oxides an additional mechanism is important in removal of atoms and ions from surfaces: potential sputtering is attributed to ejection due to the potential energy of ionization carried by ions, and is the dominant sputtering process on insulating surfaces for highly charged ions impacting with kinetic energies < 25 keV/amu [*Barghouty et al.*, 2011]. *Barghouty et al.* [2011] calculated the kinetic sputter yield in atoms/ion by solar wind protons and heavy ions at 1 keV/amu as simulated by the SRIM/TRIM code. They then calculated the enhanced sputtering due to the potential energy of ionization. This potential energy of ionization was found to increase the yield by a factor of 1.3 to 1.9 depending on the species. Because the yield depends on both the incoming ion and outgoing ion, we have taken the kinetic yield of a given species by heavy ions in the solar wind to be the average of the yield of that species from all heavy ion species in the solar wind. We used equation 2 from *Barghouty et al.* [2011] to calculate the potential sputter yield, except that we assumed the same alpha and beta for all elements. We added the potential yield thus calculated to the kinetic sputter yield. The results are consistent with the average potential yield + kinetic yield of about 1.4 times the kinetic sputter yield alone. For He^{++} the potential sputter yield is slightly larger than the kinetic sputter yield. The increase in the sputter yield due to potential energy assumed in this paper is thus very modest and is less than a factor of 2 for all elements. Table 7 lists the sputter yield of neutrals (atom/ion) by protons, by He^{++} and heavy ions weighted by the proton yield. Table 8 gives the flux (cm^{-2} s^{-1}) of neutral elements resulting from kinetic plus potential sputtering of a KREEP (K (potassium), Rare Earth Elements, and P (phosphorus) –rich basaltic soil [*Heiken et al.*, 1991]) for slow wind, fast wind, and the 3 CME components as listed in Table 5; with the corresponding flux for kinetic sputtering only in parenthesis.

[38] *Meyer et al.* [2011] obtained an 80-fold increase in sputter yield of O by Ar^+ over that from production by protons, and an additional factor of two for incident Ar^{+9} based on sputter yield of O from JSC-1A AGGL for a pressed sample lunar simulant. The sputter yield of O by 4 keV He^+ ions was given by *Dukes et al.* [2011] as 0.37. This is roughly an order of magnitude larger than the sputter yield of O by protons. Our yields for He^{++} as a fraction of proton yields range from 12.9 to 14.9 and our yields for heavy ions as a fraction of proton yields range from 61 to 83.

[39] The calculated sputter yields for the impact of ions onto leaded glass by *Shemansky* [2003] are much greater than those used here. The sputter yield of O^{+7} given by Shemansky is about two orders of magnitude greater than that of O^+; thus his calculated yield of O^{+7} relative to the yield of H^+ is about 2500 for 1 keV/amu ions. He calculates that the relative sputtering yield of solar wind ions onto

Table 7. Sputter Yield of Neutrals (Atom/Ion) of a KREEP Surface by Solar Wind Protons, Helium and Heavy Ions

Element	Na	Mg	Al	Si	K	Ca	Ti	Fe	Mn	O
Yield(H^+)	2.6E-4	2.4E-3	1.7E-3	3.9E-3	8.6E-5	2.9E-3	5.4E-4	1.3E-3	4.3E-5	2.4E-2
Yield(He^{++}/H^+)	13.1	12.8	14.2	14.5	14.9	12.7	14.4	13.6	14.5	12.9
Yield(heavy/H^+)	73	71	79	80	77	74	83	70	61.5	80

Table 8. Flux (cm^{-2} s^{-1}) of Neutral Elements Resulting From Kinetic Plus Potential Sputtering (Kinetic Only) of a KREEP Soil for Slow Wind, Fast Wind, and the 3 CME Components as Defined in Table 5

Species	Slow Wind	Fast Wind	Shock	Magnetic Bubble	CME
Na	9.0E4(7.3E4)	7.5E4(6.6E4)	3.2E5(3.2E5)	1.4E5(1.0E5)	4.9E6(3.2E6)
Mg	8.2E5(6.7E5)	6.9E5(6.1E5)	2.9E6(2.9E6)	1.3E6(9.3E5)	4.4E7(2.9E7)
Al	6.1E5(4.8E5)	5.0E5(4.4E5)	2.1E6(2.1E6)	9.7E5(6.6E5)	3.5E7(2.1E7)
Si	1.4E6(1.1E6)	1.1E6(9.8E5)	4.7E6(4.7E6)	2.2E6(1.5E6)	7.9E7(4.7E7)
K	3.1E4(2.4E4)	2.6E4(2.2E4)	1.0E5(1.0E5)	4.9E4(3.3E4)	1.8E6(1.0E6)
Ca	9.8E5(8.0E5)	8.2E5(7.3E5)	3.5E6(3.5E6)	1.5E6(1.1E6)	5.3E7(3.5E7)
Ti	2.0E5(1.5E5)	1.6E5(1.4E5)	6.7E5(6.6E5)	3.1E5(2.1E5)	1.1E7(6.6E6)
Fe	4.7E5(3.8E5)	3.9E5(3.4E5)	1.6E6(1.6E6)	7.2E5(5.2E5)	2.5E7(1.6E7)
Mn	1.5E4(1.2E4)	1.3E4(1.1E4)	5.3E4(5.2E4)	2.3E4(1.7E4)	8.2E5(5.2E5)

leaded glass is heavily weighted by the heavy ions, which are twice as efficient as protons even when weighted by their relative abundance in the solar wind.

[40] The flux of neutral elements resulting from sputtering of a KREEP soil for slow wind, fast wind, shock, magnetic bubble gas and CME driver gas are listed in Table 8. The yields have been weighted by the yield per incident ion type and the fraction of that ion in the solar wind as listed in Table 7. The yield (H$^+$) is the yield for sputtering by protons and is taken from *Barghouty et al.* [2011, Table 3]. The yield (He^{++}/H$^+$) is the yield relative to H$^+$ of each species from the He^{++} ion in the solar wind, and the yield (Heavy/H$^+$) is the weighted yield relative to H$^+$ from all ions heavier than He for the designated species. The yields differ because they are weighted by the composition.

[41] The sputter yield of secondary ions by protons is taken from *Elphic et al.* [1991]. The yield from He^{++} is taken to be a factor of 10 higher than that for protons, and that for heavy ions is taken to be a factor of 160 over that for protons. These yields are multiplied by the solar wind flux to obtain the flux of each species of secondary ion by sputtering (Table 9). These values are not used in our simulations since we only simulate the neutral exosphere, but they are used in the accompanying papers (Krauss-Varban and Travnicek, submitted manuscript, 2012). The sputter yield of secondary ions by He^{++} is taken to be a factor of ten times that for H$^+$; however the secondary ion flux for incident H$^+$ and for incident He$^+$ appear to be similar even though secondary ion yields for other elements lie on a power law curve as a function of nuclear stopping power [*Elphic et al.*, 1991]. Oxygen is not listed in Table 9 because there is not a measurable flux of O$^+$ secondary ions. Because the O ionization energy is relatively large, 13.6 eV, and the ionization probability depends exponentially on ionization energy, we expect the relative secondary ion yield for O$^+$/Na$^+$ to be on the order of 10^{-7}, extending the curve given by *Elphic et al.* [1991, Figure 3]. It is likely that the copious amounts of O$^+$ observed near the Moon originated at the Earth.

4. Simulations

[42] To investigate the effect of a CME passage at the Moon we ran simulations for an ion-sputtering source, impact vaporization source, and PSD source. We considered models for Na, K, Ca and Mg, elements predicted to be observable in the lunar exosphere by instruments on the LADEE spacecraft [*Sarantos et al.*, 2012].

4.1. Sodium

[43] The Na exosphere has been observed at the Moon and has been shown to be variable. Our simulations for the lunar sodium exosphere are shown in Figure 1, due to sputtering by a CME (Figure 1, left) and slow solar wind (Figure 1, right). Figure 1 assumes that the atmosphere is in steady state. Both Figures 1 (left) and 1 (right) contain the same steady state PSD and impact vaporization background sodium atmospheres in addition to the different sputtered components. The source rates are listed in Table 4. Figure 1 (top) shows density as a function of longitude and distance from the Moon with the Sun at the right. Figure 1 (bottom) shows column abundance projected onto the surface with the subsolar point at the center. We assumed that Na atoms stick for T < 200 K, and otherwise are re-emitted. Of the particles that stick, 50% of the atoms are re-emitted when the surface warms up to 200 K again.

[44] For the slow solar wind case (Figure 1, right), the steady state distribution for sputtering using the slow solar wind source rate is included. For the CME case (Figure 1, left), the steady state distribution from sputtering using the peak CME sputtering yields is added to the PSD and impact vaporization background. The increased sputtering yield from the ICME has two effects. First, the total Na atmospheric content is increased 14.5 times the ambient atmosphere. Second, the scale height of the atmosphere increases owing to the increase in higher energy sodium atoms from sputtering relative to PSD.

[45] CME conditions typically persist for a few days when an ICME encounters the Moon. Thus we investigate a time dependent case that shows how the exosphere evolves from the slow solar wind state to the enhanced CME state. In

Table 9. Sputter Yield of Secondary Ions (Ion/Proton) of a KREEP Surface per Incoming Proton, He^{++} and Heavy Ion

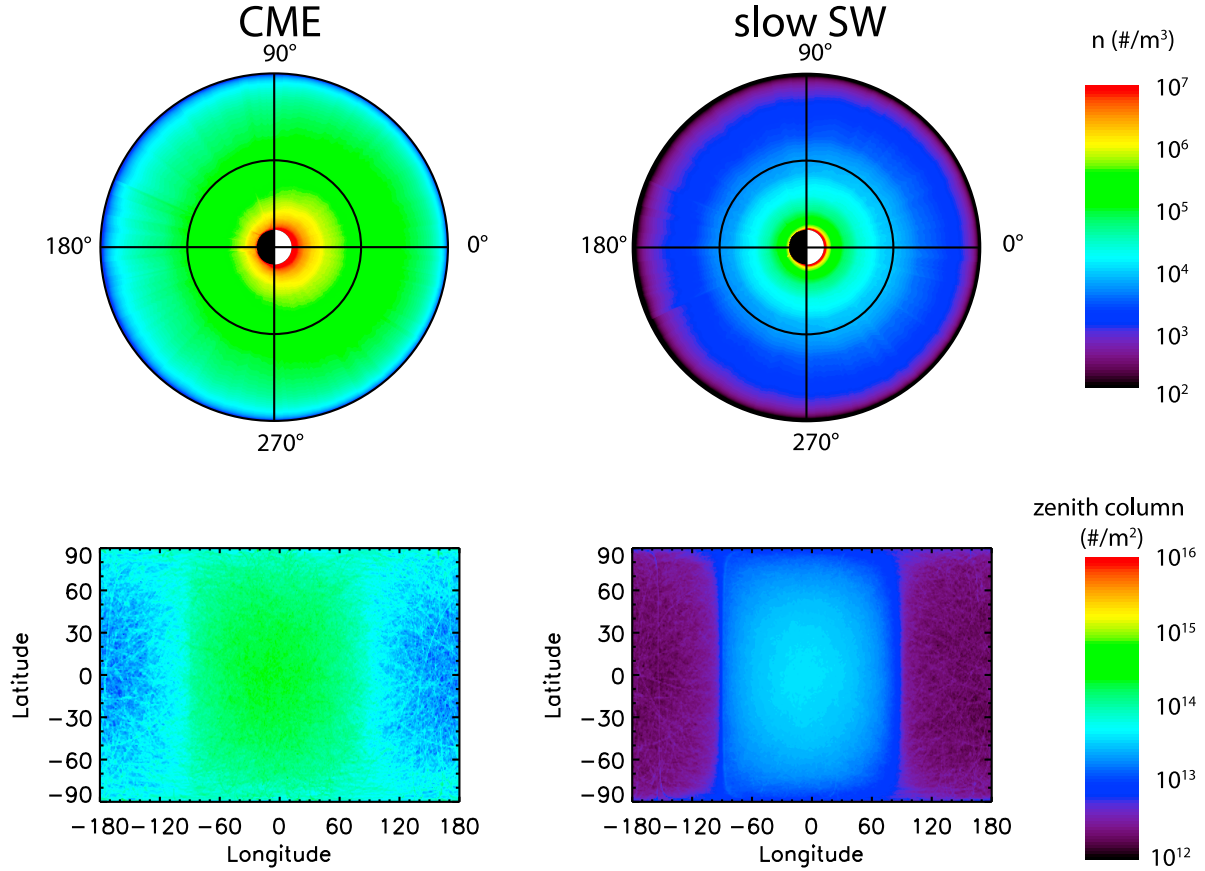| Element	Yield/H$^+$	Yield(He^{++})	Yield(heavy)
Na	8E-6	8E-5	1.3E-3
Mg	1E-5	1E-4	1.6E-3
Al	2E-5	2E-4	3.2E-3
Si	6E-5	6E-4	9.6E-3
K	3E-6	3E-5	4.8E-4
Ca	2.E-5	2.E-4	3.2E-3
Ti	1.E-6	1.E-5	1.6E-4
Fe	3.E-6	3.E-5	4.8E-4
Mn	2.E-7	2.E-6	3.2E-5
O	-	-	-

Figure 1. Simulations for the composite lunar sodium exosphere due to sputtering by (left) a CME and (right) slow solar wind. Both left and right sides contain the same steady state PSD and impact vaporization background sodium atmospheres in addition to the different sputtered components. We assumed that Na atoms stick for $T < 200$ K, and otherwise are re-emitted. (top) Density in the equatorial plane as a function of distance from the center of the Moon, with the sun at the right. Circles show the locations of 5 and 10 R_{Moon}. (bottom) Column abundance projected onto the surface with the subsolar point at the center. The atmospheric mass of Na is enhanced by a factor of 14.5 during the CME relative to that in the normal solar wind.

these time-dependent runs, the source rate is elevated for a 2-day duration to approximate the passage of the ICME. Figure 2 shows the total atmospheric mass of sodium (and other constituents discussed later) as a function of time during the passage of the 48-h ICME. Because it takes longer than 2 days for all sputtered sodium atoms to be removed from the lunar system, the total sodium mass continues to increase throughout the event, although it does not increase much after the first several hours. If CME conditions had a longer duration, the exosphere would continue to approach the steady state ICME simulation in Figure 1 (left). As the ICME turns off, there is a rapid decline in the sodium atmosphere.

[46] The auxiliary material contains movies of the time-evolution of the atmospheric enhancement for the passing ICME.[1] Movies of the time-dependent runs for Na, K, Ca

and Mg, both for the sputter component alone (Movies S1, S2, S3, and S4) and for the sum of all components including sputter, PSD, and impact vaporization (Movies S5, S6, S7, and S8), are provided. The color scale is the same for each movie, and is identical to the color scale in Figure 1. The movies show the density averaged over $\pm$ 10° latitude as a function of longitude and distance from the center of the Moon, with the Sun on the right (identical Figure 1 (top)). Because sputtering is an energetic process, >95% of the sodium ejected by the CME escapes the Moon or is photoionized. At the Hill radius, 84% reaches that distance without being photoionized, and 11% is photoionized before reaching the Hill radius. Some (<5%) recycling within the regolith occurs with the sticking and re-release selected for these runs, as likely occurs on the Moon.

4.2. Potassium

[47] Simulations for the lunar potassium exosphere due to sputtering in steady state by a CME (Figure 3, left) and slow
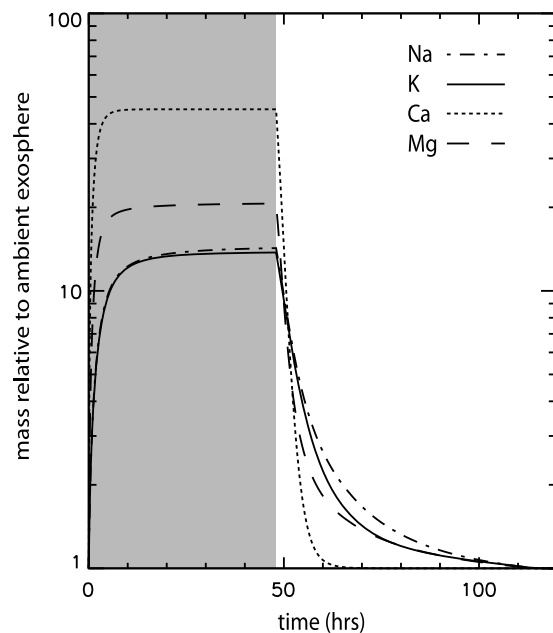
Figure 2. Time-dependent simulations were performed for enhanced sputtering from a 2-day ICME. The shaded region shows when the sputtering source rate is enhanced. The mass of each constituent as a function of time is shown relative to its ambient exospheric mass. The time-dependent runs are illustrated in two-dimensional projection in the movies in the auxiliary material. Movies S1, S2, S3 and S4 illustrate the time evolution of the sputter component of the Na, K, Ca and Mg exospheres, respectively. Movies S5, S6, S7 and S8 for Na, K, Ca and Mg, respectively, illustrate the time dependent evolution of the exospheres including the steady state background PSD (for Na and K only) and impact vaporization components with the time-dependent sputter component co-added.

solar wind (Figure 3, right), are plotted in Figure 3. The coordinate systems and the color bar are the same as described above for sodium (Figure 1). We assumed that K atoms stick for T < 200 K and that 100% of the atoms that stick to the surface are re-emitted. This assumption of sticking and re-emission causes the dawnside enhancement (left side of bottom panels above, at −90 longitude), which would occur for Na under the same assumptions. Under steady state CME conditions, the total atmospheric content is 14.7 times that of the ambient K atmosphere.

[48] For the 2-day CME run, the total mass of K in the atmosphere follows a pattern similar to Na (Figure 2). For both Na and K, the decline in atmospheric mass takes longer than the ramp-up due to the recycling in the regolith included in the simulations. See also auxiliary material, Movies S1 and S5 (Na) and Movies S2 and S6 (K).

[49] The photoionization rate for K is much larger than for Na. In addition, the heavier mass of K makes ejected atoms slower than Na. Together, this causes a much greater portion, 45% of K, to be photoionized before reaching the Hill sphere. These ions subsequently are picked up by the solar wind. Some are driven back to the surface, depending on the location of ionization and the direction of the motional electric field.

4.3. Calcium

[50] Figure 4 shows the simulations for the lunar calcium exosphere for the CME (Figure 4, left) and slow solar wind (Figure 4, right) plotted as for sodium. We assumed that any Ca atom that reencounters the surface sticks to the surface with unit efficiency. Note that in comparing CME sputtering and nominal solar wind sputtering, this choice was not very important because < 1% of the sputtered particles actually returned to the surface. However, the Ca released by impact vaporization is not energetic enough to escape the Moon. Therefore the choice of sticking affects the background atmosphere substantially. The CME causes a much more extended and denser exosphere than the slow solar wind. The high sputtering yields for Ca produce an atmospheric enhancement of 44 times the nominal mass of Ca during a prolonged sputtering event on the Moon, based on the calculated sputtering yield enhancements from the energetic component of the ICME flux.

[51] For the time dependent case, the ramp up and ramp down times are much shorter for Ca than for Na and K. Na and K are less strongly bound to the surface than Ca and Mg. Thus the energy of sputtered Ca and Mg is greater than sputtered Na and K (equation (3)). It only takes 38 min for half of the Ca particles to reach 10 R_{Moon}, compared to 67 min for Na. In contrast to Na and K, the total amount of Ca in the exosphere is back down to the background level within a few hours of the end of CME conditions (see the auxiliary material, Movies S3 and S7).

[52] The effect of the CME on the total mass of Ca in the exosphere is greater than for Na and K by a factor of about 3. This is because there is no PSD component of Ca in the exosphere. PSD is the dominant source in steady state conditions for Na and K. Thus, the sputtered component is a greater percentage of the total exosphere for Ca, and its resulting increase during a CME has a greater relative effect.

4.4. Magnesium

[53] Simulations for the lunar magnesium exosphere for the CME (Figure 5, left) and slow solar wind (Figure 5, right) are plotted in Figure 5. We assumed that 100% of Mg atoms that reencounter the surface stick are not re-emitted. The magnesium exosphere is more extended than sodium due to its larger binding energy with the surface. The CME causes a much more extended exosphere than the slow solar wind, and a factor of 21 increase in the number of magnesium atoms in the exosphere. The magnesium is similar to calcium due to its similar binding energy with the surface, but its scale height is larger due to its lesser mass. The time evolution of the Mg content of the atmosphere during the time dependent run is also similar to Ca, owing to the high velocity of the sputtered atoms, but it takes the longest to decay owing to its low mass, high velocity and very long photoionization lifetime (see the auxiliary material, Movies S4 and S8). Like Ca, Mg lacks a PSD component to the exosphere, which lends a greater relative contribution from the sputtered component. The lifetime of Mg due to photoionization is 204 days, thus photoionization can be neglected for this species.

5. Discussion

[54] Using observations of the lunar atmosphere when the Moon is inside and outside of the Earth's magnetosphere,
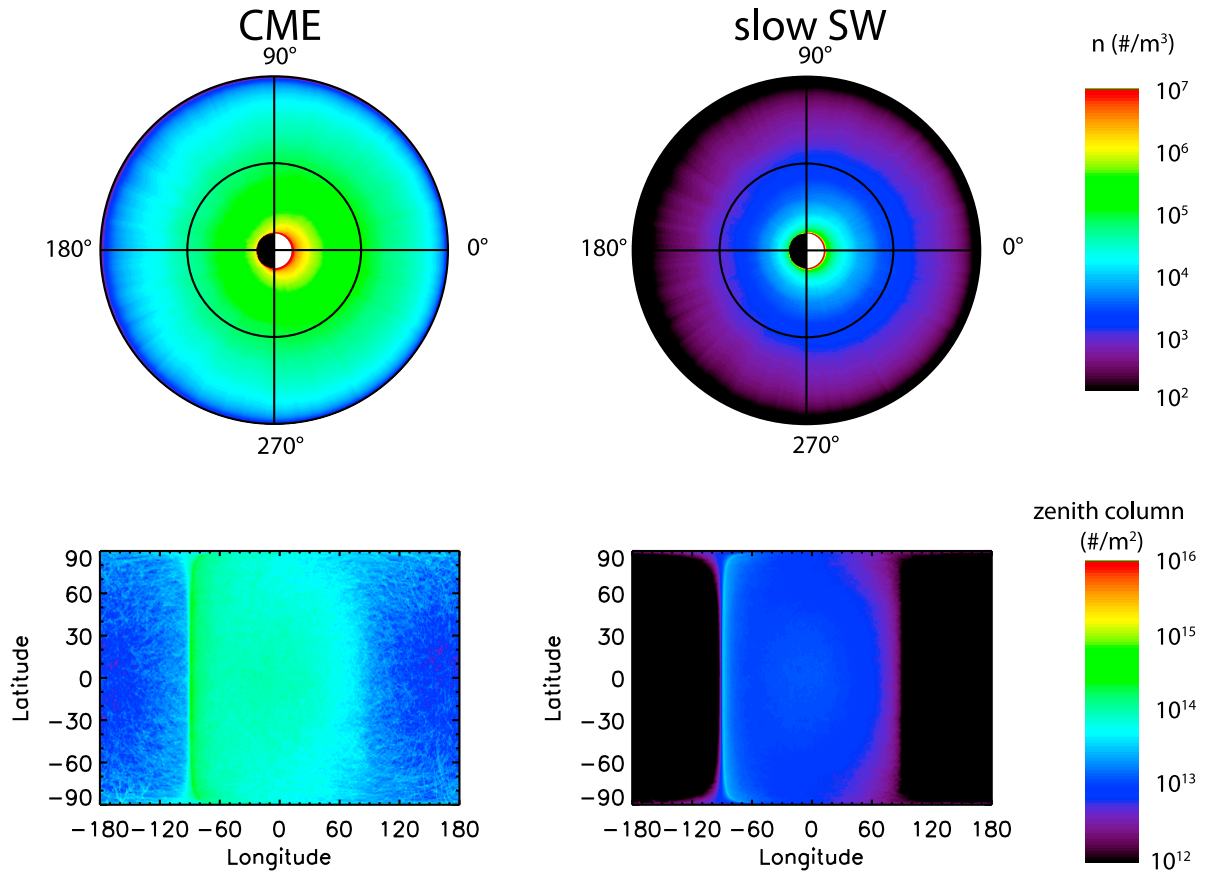
Potassium

Figure 3. Simulations for the lunar potassium exosphere due to sputtering by (left) a CME and (right) slow solar wind, plotted as for sodium. We assumed that K atoms stick for T < 200 K and that 100% of the atoms that stick to the surface are re-emitted. This assumption of sticking and re-emission causes the dawnside enhancement (Figure 3, bottom left, at −90 longitude), which would occur for Na under the same assumptions. The atmospheric mass of K is enhanced by a factor of 14.7 during the CME passage over that in the slow solar wind.

respectively, *Mendillo et al.* [1999] concluded that solar wind sputtering is not a significant source of the Na atmosphere of the Moon. Using estimates of the solar wind density, velocity and composition in the slow solar wind and a CME, we have estimated that a > 10 fold increase in the lunar exospheric density due to sputtering alone could result from a CME passage through the influence of sputtering by highly charged ions, including He^{++} that may be highly enriched in the CME plasma. *Wurz et al.* [2007] argue that the potential sputter enhancement is strongly dependent upon the ion dose and, after a removal of about a monolayer from the oxide surface, the sputter yield for highly charged ions drops to about the values for singly charged ions. As discussed by *Barghouty et al.* [2011], there was no metalization effect observed in their measurements of sputtering by highly charged ions, thus the preferential removal of oxygen from a surface monolayer is most likely not occurring on the lunar surface as proposed by *Wurz et al.* [2007]. Also, as discussed by *Killen et al.* [2004] ion-enhanced diffusion will act to replenish the surface monolayer. The characteristic timescale for an element to reach steady state in a normal

solar wind is about 1200 years, which is the timescale for a 1 mm layer to be overturned on the lunar surface. Thus fresh material is exposed by gardening, and brought to the surface by diffusion on timescales shorter than timescales on which the elemental abundance reaches its yield-weighted fractional abundance. Observations of the lunar exosphere during an extended period of time, especially during solar maximum, could be of use in testing this hypothesis.

6.   Conclusions

[55] Our simulations indicate that sputtering by the enhanced highly charged heavy ions in the plasma associated with a CME can enhance the lunar exosphere content due to sputtering by approximately a factor of >10, depending on the species. The enhanced flux in the CME plasma is an additional important factor in enhancing the total sputter yield. The solar wind density and velocity are being monitored by the STEREO spacecraft, and the heliosphere can be modeled using the community model center at Goddard Space Flight Center. Future observations of the
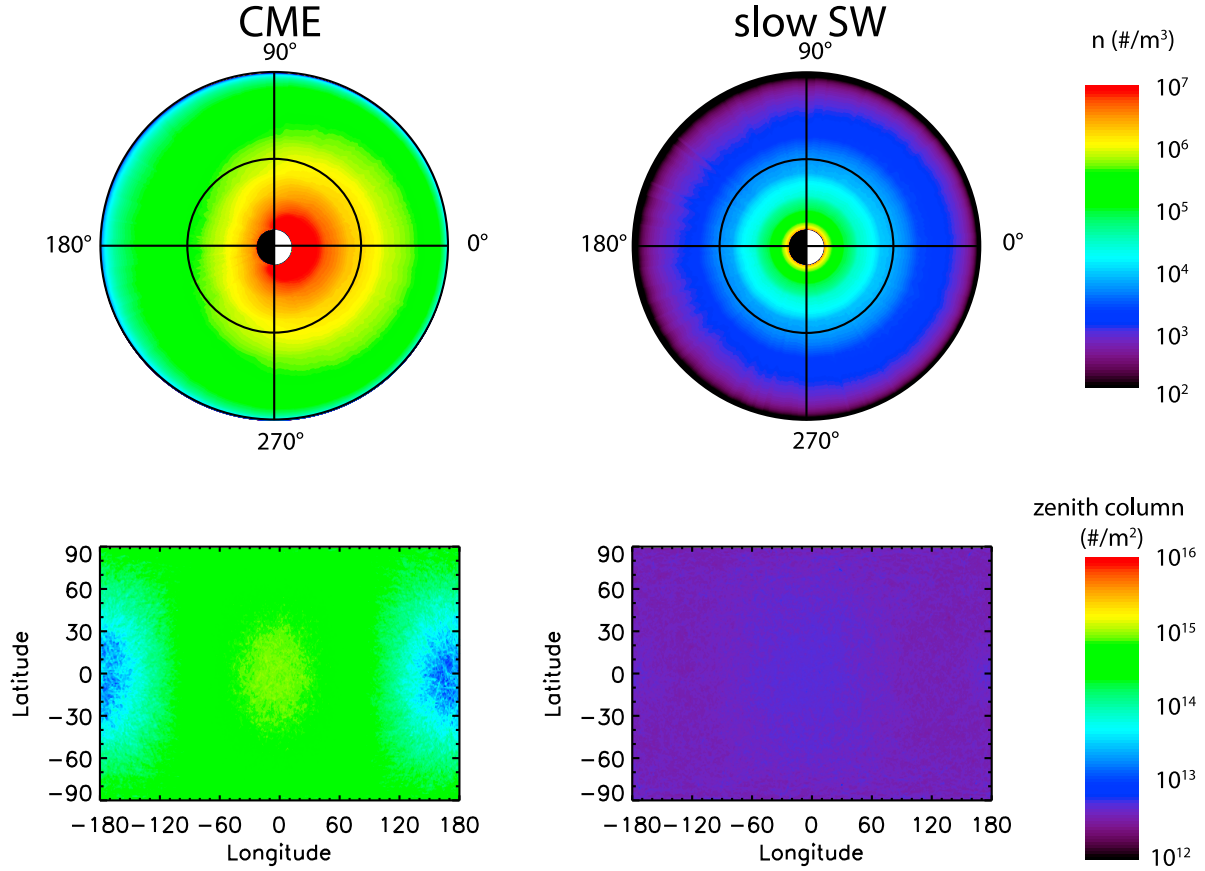
Figure 4. Simulations for the lunar calcium exosphere for (left) the CME and (right) slow solar wind plotted as for sodium. We assumed that Ca atoms stick to the surface with unit efficiency. Photon-stimulated desorption is not energetic enough to eject calcium or magnesium, but impact vaporization is included. The CME produces a much denser exosphere than the slow solar wind. The enhancement in atmospheric mass of Ca during the CME is a factor of 44 over that in the slow solar wind.

lunar exosphere can be used, along with measurements of the solar wind, to test these results. The Lyman Alpha Mapping Project (LAMP) onboard the Lunar Reconnaissance Orbiter is conducting observations of the atmosphere that will further constrain the amounts of Mg and Ca in the lunar atmosphere. LAMP observations in conjunction with these simulations can verify the source rates for those species in the lunar exosphere. The Lunar Atmosphere and Dust Environment Explorer (LADEE) spacecraft will also observe the atmosphere of the Moon. Its planned launch in 2013 places the mission during solar maximum. Species expected to reside in the lunar exosphere normally just below levels of detectability for a 1-s integration by the LADEE UV spectrometer (Ca, Mg, and Al) [*Sarantos et al.*, 2012] will be elevated above the limit of detectability during the passage of a CME. Provided that the instrument can operate with elevated particle fluxes, we will spatially resolve all of these species rather than just "smear" them spatially in order to detect them. Likewise, species predicted to normally exist in the lunar exosphere at levels just below detectability by the LADEE Neutral Mass Spectrometer (Si, O and Al) [*Sarantos et al.*, 2012] should be elevated above

minimum detectable limits during the CME passage. Thus LADEE will provide crucial data to test these predictions through the neutral mass spectrometer and the UV spectrometer. Furthermore, LADEE will likely observe the Moon as it passes through a meteor shower, allowing it to quantify the contribution of impact vaporization to the exosphere by observing the enhancement from a sudden increase in the impact vaporization rate. This model can be used to simulate that process as well.

[56] The enhanced exosphere from a CME increases the amount of photoions near the Moon. Additionally, sputtering ejects a small percentage of species as ions [*Elphic et al.*, 1991]. The results of this work feed into the hybrid plasma calculations of Krauss-Varban and Travnicek (submitted manuscript, 2012). Picked-up ions were detected downstream of the Moon by AMPTE and WIND [*Hilchenbach et al.*, 1993; *Mall et al.*, 1998]. More recently, *Yokota et al.* [2009] have detected photoions and sputtered ions, including H^+, He^{++}, He^+, C^+, O^+, Na^+, K^+, and Ar^+, close to the Moon with Kaguya.

[57] From a global perspective, the increase sputtering rates during a CME passage amounts to an overall temporary
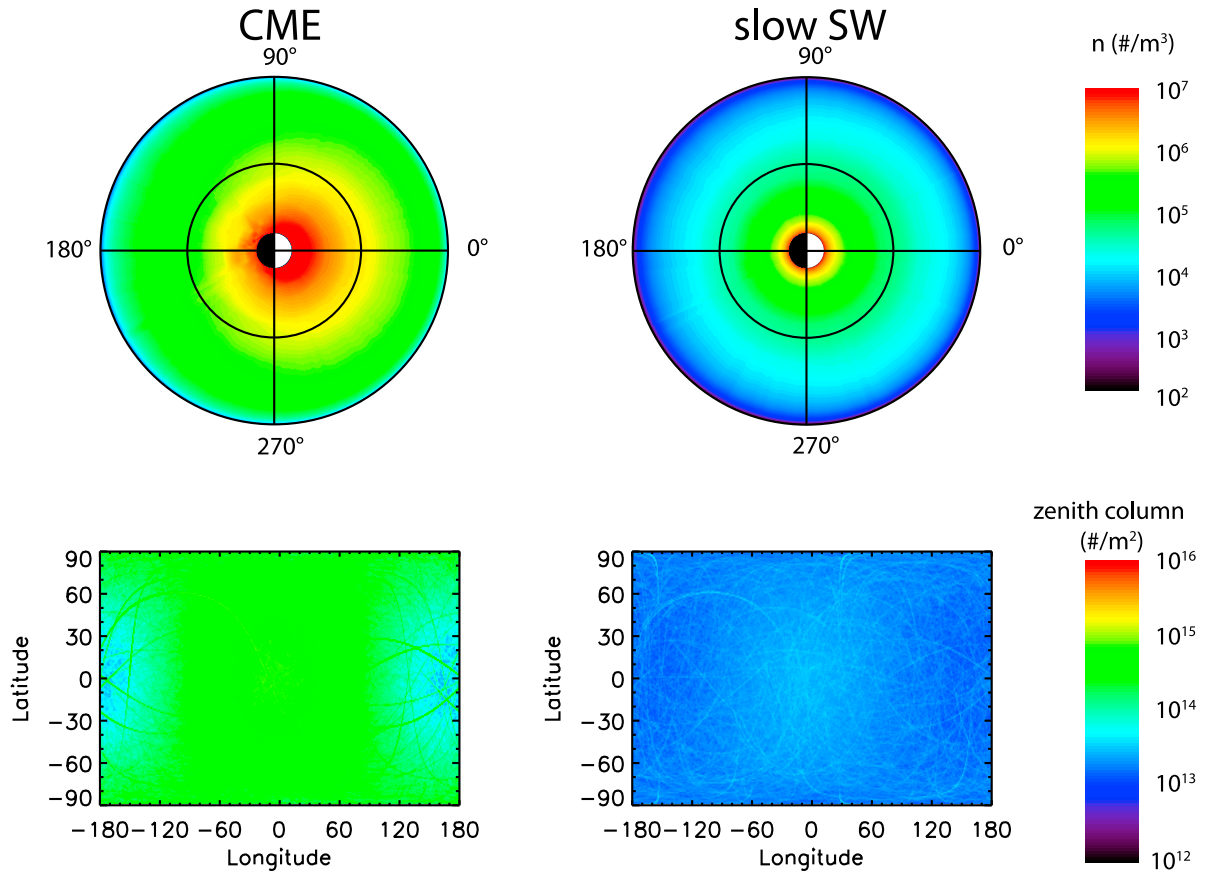
Figure 5. Simulations for the lunar magnesium exosphere for (left) the CME and (right) slow solar wind plotted as for sodium. We assumed that Mg atoms stick to the surface with unit efficiency. The magnesium is more extended than sodium due to its larger binding energy with the surface, which results in a higher ejection velocity. The CME causes a much denser exosphere than the slow solar wind; the atmospheric mass of Mg is enhanced by a factor of 21 during the CME. Note that there is little difference between the slow and fast solar wind in terms of sputtering efficiency. The magnesium is similar to calcium due to its similar binding energy with the surface, but its scale height is larger due to its lesser mass.

increase in regolith-species mass loss from the Moon. For example, Ca surface sputtering rates are $\sim 0.5 \times 10^{12}$ atoms m^{-2}-s^{-1}. When integrated over the dayside surface area of $\sim 2 \times 10^{13}$ m^2, this rate amounts to an overall sputtering loss of close to $\sim 10^{25}$ atoms/s, or ~ 0.5 kg/s. Assuming 50% fully escape (a low estimate for Ca), this sputtering amounts to 0.25 kg/s of instantaneous Ca loss and over 40 tons of Ca lost over a two day CME passage like that of 2 May 1998. A similar argument made for Si, Al, Fe, and the species shown in Table 8 results in an overall mass loss that should exceed 100 tons of material during the CME passage. We note that a similar amount of material, ~ 200 tons, is delivered directly to the lunar surface in the form of CME protons and heavy multicharged ions. However, the incoming momentum of this sun-originating ion flow is transferred to outgoing lunar-originating neutrals removed from the regolith and this transfer becomes highly efficient during the passage of the CME driver plasma.

References

Ahrens, T. J., and J. D. O'Keefe (1972), Shock melting and vaporization of lunar rocks and minerals, *Moon*, *4*, 214–249, doi:10.1007/BF00562927.

Arnold, J. R. (1979), Ice in the lunar polar regions, *J. Geophys. Res.*, *84*(B10), 5659–5668, doi:10.1029/JB084iB10p05659.

Aumayr, F., and H. Winter (2004), Potential sputtering, *Philos. Trans. R. Soc. London, Ser. A*, *362*, 77–102, doi:10.1098/rsta.2003.1300.

Barghouty, A. F., F. W. Meyer, P. R. Harris, and J. H. Adams Jr. (2011), Solar-wind protons and heavy ions sputtering of lunar surface materials, *Nucl. Instrum. Methods Phys. Res., Sect. B*, *269*, 1310–1315, doi:10.1016/j.nimb.2010.12.033.

Bida, T., R. M. Killen, and T. H. Morgan (2000), Discovery of Ca in the atmosphere of Mercury, *Nature*, *404*, 159–161, doi:10.1038/35004521.

Butler, B. J. (1997), The migration of volatiles on the surfaces of Mercury and the Moon, *J. Geophys. Res.*, *102*(E8), 19,283–19,291, doi:10.1029/97JE01347.

Carter, J. A., S. Sembay, and A. M. Read (2010), A high charge state coronal mass ejection seen through solar wind charge exchange emission as detected by XMM-Newton, *Mon. Not. R. Astron. Soc.*, *402*, 867–878, doi:10.1111/j.1365-2966.2009.15985.x.

Cassidy, T. A., and R. E. Johnson (2005), Monte Carlo model of sputtering and other ejection processes within a regolith, *Icarus*, *176*(2), 499–507, doi:10.1016/j.icarus.2005.02.013.

Chang, J.-J., and H. P. Kelly (1975), Photoabsorption of the neutral sodium atom: A many-body calculation, *Phys. Rev. A*, *12*, 92–98, doi:10.1103/PhysRevA.12.92.

Chase, M. W., Jr. et al. (Eds.) (1985), JANAF thermochemical tables, *J. Phys. Chem. Ref. Data*, *14*, suppl. 1, 685–711, 1567–1598, 1786–1792, 1795.

Cintala, M. J. (1992), Impact-induced thermal effects in the lunar and Mercurian regoliths, *J. Geophys. Res.*, *97*(E1), 947–973, doi:10.1029/91JE02207.

Cladis, J. B., W. E. Francis, and R. R. Vondrak (1994), Transport toward earth of ions sputtered from the Moon's surface by the solar wind, *J. Geophys. Res.*, *99*(A1), 53–64, doi:10.1029/93JA02672.

Combi, M. R., M. A. Disanti, and U. Fink (1997), The spatial distribution of gaseous atomic sodium in the comae of comets: Evidence for direct nucleus and extended plasma sources, *Icarus*, *130*, 336–354, doi:10.1006/icar.1997.5832.

Cremonese, G., M. Bruno, V. Mangano, S. Marchi, and A. Milillo (2005), Release of neutral sodium atoms from the surface of Mercury induced by meteoroid impacts, *Icarus*, *177*, 122–128, doi:10.1016/j.icarus.2005.03.022.

Crider, D. H., and R. R. Vondrak (2000), The solar wind as a possible source of lunar polar hydrogen deposits, *J. Geophys. Res.*, *105*(E11), 26,773–26,782, doi:10.1029/2000JE001277.

Crider, D. H., and R. R. Vondrak (2002), Hydrogen implantation and migration by solar wind bombardment of the Moon, *Adv. Space Res.*, *30*(8), 1869–1874, doi:10.1016/S0273-1177(02)00493-3.

Dukes, C. A., W.-Y. Chang, M. Famá, and R. A. Baragiola (2011), Laboratory studies on the sputtering contribution to the sodium atmospheres of Mercury and the Moon, *Icarus*, *212*(2), 463–469, doi:10.1016/j.icarus.2011.01.027.

Elphic, R. C., H. O. Funsten III, F. B. L. Barraclough, D. J. McComas, M. T. Paffett, D. T. Vaniman, and G. Heiken (1991), Lunar surface composition and solar wind-induced secondary ion mass spectrometry, *Geophys. Res. Lett.*, *18*(11), 2165–2168, doi:10.1029/91GL02669.

Gladstone, G. R., et al. (2010), LRO-LAMP observations of the LCROSS impact plume, *Science*, *330*, 472–476, doi:10.1126/science.1186474.

Gloeckler, G., L. A. Fisk, S. Hefti, N. A. Schwandron, T. H. Zurbuchen, F. M. Ipavich, J. Geiss, P. Bochsler, and R. F. Wimmer-Schweingruber (1999), Unusual composition of the solar wind in the 2–3 May 1998 CME observed with SWICS on ACE, *Geophys. Res. Lett.*, *26*(2), 157–160, doi:10.1029/1998GL900166.

Hapke, B. W., and W. A. Cassidy (1978), Is the Moon really as smooth as a billiard ball: Remarks concerning recent models of sputter-fractionation on the lunar surface, *Geophys. Res. Lett.*, *5*(4), 297–300, doi:10.1029/GL005i004p00297.

Heiken, G. H., D. T. Vaniman, and B. M. French (1991), *Lunar Sourcebook*, Cambridge Univ. Press, New York.

Hilchenbach, M., D. Hovestadt, B. Klecker, and E. Möbius (1993), Observations of energetic lunar pick-up ions near Earth, *Adv. Space Res.*, *13*(10), 321–324, doi:10.1016/0273-1177(93)90086-Q.

Hodges, R. R. (1973), Helium and hydrogen in the lunar atmosphere, *J. Geophys. Res.*, *78*(34), 8055–8064, doi:10.1029/JA078i034p08055.

Hofer, W. O. (1991), Angular energy and mass distribution of sputtered particles, in *Sputtering by Particle Bombardment III*, edited by R. Behrisch and K. Wittmaack, pp. 15–90, Springer, New York.

Hudson, R. D. (1964), Atomic absorption cross section of sodium vapor between 2400 and 1000 Å, *Phys. Rev.*, *135*, A1212–A1217, doi:10.1103/PhysRev.135.A1212.

Hudson, R. D., and V. L. Carter (1967), Experimental values of the atomic absorption cross section of potassium between 580 Angstroms and 1000 Angstroms, *J. Opt. Soc. Am.*, *57*, 1471–1474, doi:10.1364/JOSA.57.001471.

Huebner, W. F., J. J. Keady, and S. P. Lyon (1992), Solar photo rates for planetary atmospheres and atmospheric pollutants, *Astrophys. Space Sci.*, *195*, 1–294, doi:10.1007/BF00644558.

Hunten, D. M., G. Cremonese, A. L. Sprague, R. E. Hill, S. Verani, and R. W. H. Kozlowski (1998), The Leonid meteor shower and the lunar sodium atmosphere, *Icarus*, *136*, 298–303, doi:10.1006/icar.1998.6023.

Hurley, D. M. (2011), Modeling of the vapor release from the LCROSS impact: I. Parametric dependencies, *J. Geophys. Res.*, *116*, E10007, doi:10.1029/2010JE003793.

Johnson, R. E. (1990), *Energetic Charged-Particle Interactions with Atmospheres and Surfaces*, Springer, New York.

Kallio, E., and P. Janhunen (2003), Solar wind and magnetospheric ion impact on Mercury's surface, *Geophys. Res. Lett.*, *30*(17), 1877, doi:10.1029/2003GL017842.

Kallio, E., et al. (2008), On the impact of multiply charged heavy solar wind ions on the surface of Mercury, the Moon and Ceres, *Planet. Space Sci.*, *56*(11), 1506–1516, doi:10.1016/j.pss.2008.07.018.

Killen, R. M. (2003), Depletion of sulfur on the surface of asteroids and the Moon, *Meteorit. Planet. Sci.*, *38*, 383–388, doi:10.1111/j.1945-5100.2003.tb00273.x.

Killen, R. M., and W.-H. Ip (1999), The Surface-bounded atmospheres of Mercury and the Moon, *Rev. Geophys.*, *37*(3), 361–406, doi:10.1029/1999RG900001.

Killen, R. M., A. E. Potter, P. Reiff, M. Sarantos, B. V. Jackson, P. Hick, and B. Giles (2001), Evidence for space weather at Mercury, *J. Geophys. Res.*, *106*(E9), 20,509–20,525, doi:10.1029/2000JE001401.

Killen, R. M., M. Sarantos, A. E. Potter, and P. Reiff (2004), Source rates and ion recycling rates for Na and K in Mercury's atmosphere, *Icarus*, *171*, 1–19, doi:10.1016/j.icarus.2004.04.007.

Killen, R. M., et al. (2007), Processes that promote and deplete the exosphere of Mercury, *Space Sci. Rev.*, *132*, 433–509.

Killen, R. M., A. E. Potter, D. M. Hurley, C. Plymate, and S. Naidu (2010), Observations of the lunar impact plume from the LCROSS event, *Geophys. Res. Lett.*, *37*, L23201, doi:10.1029/2010GL045508.

Krachner, A., F. Aumayr, D. W. G. Sears, and M. Kareev (2003), Space weathering by highly charged heavy ions in the solar wind, Abstract 5204, presented at the 66th Annual Meteoritical Society Meeting, Munster, Germany, 28 July to 1 August.

Lange, M. A., and T. J. Ahrens (1987), Atmospheric blow-off during accretion of the terrestrial planetary atmospheres, *Icarus*, *69*, 506–518, doi:10.1016/0019-1035(87)90020-0.

Leblanc, F., and R. E. Johnson (2010), Mercury exosphere: I. Global circulation model of its sodium content, *Icarus*, *209*, 280–300, doi:10.1016/j.icarus.2010.04.020.

Mall, U., E. Kirsch, K. Cierpka, B. Wilken, A. Söding, F. Neuauer, G. Gloeckler, and A. Galvin (1998), Direct observation of lunar pick-up ions near the Moon, *Geophys. Res. Lett.*, *25*(20), 3799–3802, doi:10.1029/1998GL900003.

Mangano, V., A. Milillo, A. Mura, S. Orsini, E. deAngelis, A. M. diLellis, and P. Wurz (2007), The contribution of impulsive meteoritic impact vapourization to the Hermean exosphere, *Planet. Space Sci.*, *55*, 1541–1556, doi:10.1016/j.pss.2006.10.008.

McClintock, W. E., R. J. Vervack Jr., E. T. Bradley, R. M. Killen, N. Mouawad, A. L. Sprague, M. H. Burger, S. C. Solomon, and N. R. Izenberg (2009), Mercury's exosphere during MESSENGER's second flyby: Detection of magnesium and distinct distributions of neutral species, *Science*, *324*, 610–613.

McGrath, M. A., R. E. Johnson, and L. J. Lanzerotti (1986), Sputtering of sodium on the planet Mercury, *Nature*, *323*, 694–696, doi:10.1038/323694a0.

Melosh, H. J. (1989), *Impact Cratering: A Geologic Process*, Oxford Univ. Press, Oxford, U. K.

Mendillo, M., J. Baumgardner, and J. Wilson (1999), Observational test for the solar wind sputtering origin of the Moon's extended sodium atmosphere, *Icarus*, *137*, 13–23, doi:10.1006/icar.1998.6042.

Meyer, F. W., P. R. Harris, C. N. Taylor, H. M. Meyer III, A. F. Barghouty, and J. H. Adams (2011), Sputtering of lunar regolith simulant by protons and singly and multicharged Ar ions at solar wind energies, *Nuclear Instrum. Methods Phys. Res., Sect. B*, *269*(11), 1316–1320.

Morgan, T. H., and R. M. Killen (1998), Production mechanisms for faint but possibly detectable coronae about asteroids, *Planet. Space Sci.*, *46*, 843–850, doi:10.1016/S0032-0633(98)00029-4.

Morgan, T. H., H. A. Zook, and A. E. Potter (1988), Impact-driven supply of sodium and potassium to the atmosphere of Mercury, *Icarus*, *75*, 156–170, doi:10.1016/0019-1035(88)90134-0.

Mouawad, N., M. H. Burger, R. M. Killen, A. E. Potter, W. E. McClintock, R. J. Vervack, E. T. Bradley, M. Benna, and S. Naidu (2011), Constraints on Mercury's Na exosphere: Combined MESSENGER and ground-based data, *Icarus*, *211*, 21–36, doi:10.1016/j.icarus.2010.10.019.

Mura, A. (2011), Loss rates and timescales for sodium at Mercury, *Planet. Space Sci.*, doi:10.1016/j.pss.2011.08.012, in press.

Ogilvie, K. W., J. T. Steinberg, R. J. Fitzenreiter, C. J. Owen, A. J. Lazarus, W. M. Farrell, and R. B. Torbert (1996), Observations of the lunar plasma wake from the WIND spacecraft on December 27, 1994, *Geophys. Res. Lett.*, *23*(10), 1255–1258, doi:10.1029/96GL01069.

Okabayashi, N., K. Komaki, and Y. Yamazaki (2005), Potential sputtering and kinetic sputtering from a water adsorbed Si(1 0 0) surface with slow highly charged ions, *Nucl. Instrum. Methods Phys. Res., Sect. B*, *232*(1–4), 244–248.

Potter, A. E., and T. H. Morgan (1985), Discovery of sodium in the atmosphere of Mercury, *Science*, *229*, 651–653, doi:10.1126/science.229.4714.651.

Potter, A. E., and T. H. Morgan (1988a), Discovery of sodium and potassium vapor in the atmosphere of the Moon, *Science*, *241*, 675–680, doi:10.1126/science.241.4866.675.

Potter, A. E., and T. H. Morgan (1988b), Extended sodium exosphere of the Moon, *Geophys. Res. Lett.*, *15*(13), 1515–1518, doi:10.1029/GL015i013p01515.

Potter, A. E., and T. H. Morgan (1990), Evidence for magnetospheric effects on the sodium atmosphere of Mercury, *Science*, *248*, 835–838, doi:10.1126/science.248.4957.835.

Potter, A. E., R. M. Killen, and T. H. Morgan (2000), Variation of lunar sodium during passage of the Moon through the Earth's magnetotail, *J. Geophys. Res.*, *105*(E6), 15,073–15,084, doi:10.1029/1999JE001213.

Potter, A. E., R. M. Killen, and T. H. Morgan (2007), Solar radiation acceleration effects on Mercury sodium emission, *Icarus*, *186*, 571–580, doi:10.1016/j.icarus.2006.09.025.

Reinard, A. A. (2008), Analysis of interplanetary coronal mass ejection parameters as a function of energetics, source location, and magnetic structure, *Astrophys. J.*, *682*(2), 1289–1305, doi:10.1086/589322.

Roth, J. (1983), Chemical sputtering, in *Sputtering by Particle Bombardment II*, edited by R. Behrisch and K. Wittmaack, pp. 91–146, Springer, Berlin.

Sarantos, M., R. M. Killen, and D. Kim (2007), Predicting the solar wind ion-sputtering source at Mercury, *Planet. Space Sci.*, *55*, 1584–1595, doi:10.1016/j.pss.2006.10.011.

Sarantos, M., R. M. Killen, A. S. Sharma, and J. A. Slavin (2008), Correlation between Lunar Prospector electron flux measurements and the lunar exosphere during passage through the Earth's magnetosphere, *Geophys. Res. Lett.*, *35*, L04105, doi:10.1029/2007GL032310.

Sarantos, M., R. M. Killen, A. S. Sharma, and J. A. Slavin (2010), Sources of sodium in the lunar exosphere: Modeling using ground-based observations of sodium emission and spacecraft data of the plasma, *Icarus*, *205*, 364–374, doi:10.1016/j.icarus.2009.07.039.

Sarantos, M., R. M. Killen, D. A. Glenar, M. Benna, and T. J. Stubbs (2012), Metallic species, oxygen and silicon in the lunar exosphere: Upper limits and prospects for LADEE measurements, *J. Geophys. Res.*, doi:10.1029/2011JA017044, in press.

Schultz, P. H. (1996), Effect of impact angle on vaporization, *J. Geophys. Res.*, *101*(E9), 21,117–21,136, doi:10.1029/96JE02266.

Shemansky, D. E. (2003), The role of solar wind heavy ions in the space environment, *AIP Conf. Proc.*, *663*, 687–695, doi:10.1063/1.1581610.

Sigmund, P. (1969), Theory of sputtering: I. Sputtering yield of amorphous and polycrystalline targets, *Phys. Rev.*, *184*, 383–416, doi:10.1103/PhysRev.184.383.

Smyth, W. H., and M. L. Marconi (1995a), Theoretical overview and modeling of the sodium and potassium atmospheres of Mercury, *Astrophys. J.*, *441*, 839–864, doi:10.1086/175407.

Smyth, W. H., and M. L. Marconi (1995b), Theoretical overview and modeling of the sodium and potassium atmospheres of the Moon, *Astrophys. J.*, *443*, 371–392, doi:10.1086/175532.

Snow, M., et al. (2005), The LASP Interactive Solar Irradiance Datacenter (LISIRD), *EOS Trans. AGU*, *86*(52), Fall Meet. Suppl., Abstract IN33B-1180.

Sporn, M., G. Libiseller, T. Neidhart, M. Schmid, F. Aumayr, H. P. Winter, P. Varga, M. Grether, D. Niemann, and N. Stolterfoht (1997), Potential sputtering of clean SiO$_2$ by slow highly charged ions, *Phys. Rev. Lett.*, *79*, 945–948, doi:10.1103/PhysRevLett.79.945.

Stern, S. A. (1999), The lunar atmosphere: History, status, current problems, and context, *Rev. Geophys.*, *37*(4), 453–491, doi:10.1029/1999RG900005.

Verner, D. A., G. J. Ferland, K. T. Korista, and D. G. Yakovlev (1996), Atomic data for astrophysics. II. New analytic fits for photoionization cross sections of atoms and ions, *Astrophys. J.*, *465*, 487–498, doi:10.1086/177435.

Vogel, U. (1966), Molecular fluxes in the lunar atmosphere, *Planet. Space Sci.*, *14*, 1233–1252, doi:10.1016/0032-0633(66)90078-X.

Vondrak, R. R. (1992), Lunar base activities and the lunar environment, *NASA Conf. Publ.*, *3166*, 337–345.

von Steiger, R., N. A. Schwadron, L. A. Fisk, J. Geiss, S. Hefti, B. Wilken, R. F. Wimmer-Schweingruber, and T. H. Zurbuchen (2000), Composition of the quasi-stationary solar wind flows from Ulysses/Solar Wind Ion Composition Spectrometer, *J. Geophys. Res.*, *105*(A12), 27,217–27,238, doi:10.1029/1999JA000358.

Winske, D., C. S. Wu, Y. Y. Li, Z. Z. Mou, and S. Y. Guo (1985), Coupling of newborn ions to the solar wind by electromagnetic instabilities and their interaction with the bow shock, *J. Geophys. Res.*, *90*(A3), 2713–2726, doi:10.1029/JA090iA03p02713.

Wurz, P., and H. Lammer (2003), Monte Carlo simulation of Mercury's exosphere, *Icarus*, *164*, 1–13, doi:10.1016/S0019-1035(03)00123-4.

Wurz, P., et al. (1997), Elemental composition before, during, and after the January 6, 1997 CME event measured by CELIAS/SOHO, *Eur. Space Agency Spec. Publ.*, *ESA SP-415*, 395–400.

Wurz, P., P. Bochsler, and M. A. Lee (2000), Model for the mass fractionation in the January 6, 1997 coronal mass ejection, *J. Geophys. Res.*, *105*(A12), 27,239–27,250, doi:10.1029/2000JA900120.

Wurz, P., U. Rohner, J. A. Whitby, C. Kolb, H. Lammer, P. Dobniker, and J. A. Martin-Fernandez (2007), The lunar atmosphere: The sputtering contribution, *Icarus*, *191*, 486–496, doi:10.1016/j.icarus.2007.04.034.

Yakshinskiy, B. V., and T. E. Madey (1999), Photon-stimulated desorption as a substantial source of sodium in the lunar atmosphere, *Nature*, *400*, 642–644, doi:10.1038/23204.

Yokota, S., et al. (2009), First direct detection of ions originating from the Moon by MAP-PACE IMA onboard SELENE (KAGUYA), *Geophys. Res. Lett.*, *36*, L11201, doi:10.1029/2009GL038185.

W. M. Farrell and R. Killen, Planetary Magnetospheres Branch, NASA Goddard Space Flight Center, Code 695, Greenbelt, MD 20771, USA. (rosemary.killen@nasa.gov)

D. M. Hurley, Johns Hopkins University Applied Physics Laboratory, MP3-E169, 11100 Johns Hopkins Rd., Laurel, MD 20723, USA.